LIVERPOOL JOHN MOORES UNIVERSITY

LJMU Research Online

Ye, Y, Gan, J, Liu, H, Wu, W, Wang, L, Guo, J and Li, H

Bending behaviour of rigid-flexible combined inflatable membrane structures for floating bridge modules

https://researchonline.ljmu.ac.uk/id/eprint/27333/

Article

Citation (please note it is advisable to refer to the publisher's version if you intend to cite from this work)

Ye, Y ORCID logoORCID: https://orcid.org/0000-0003-2797-2304, Gan, J, Liu, H, Wu, W, Wang, L, Guo, J and Li, H ORCID logoORCID: https://orcid.org/0000-0001-6429-9097 (2025) Bending behaviour of rigid-flexible combined inflatable membrane structures for floating bridge

LJMU has developed **LJMU Research Online** for users to access the research output of the University more effectively. Copyright © and Moral Rights for the papers on this site are retained by the individual authors and/or other copyright owners. Users may download and/or print one copy of any article(s) in LJMU Research Online to facilitate their private study or for non-commercial research. You may not engage in further distribution of the material or use it for any profit-making activities or any commercial gain.

The version presented here may differ from the published version or from the version of the record. Please see the repository URL above for details on accessing the published version and note that access may require a subscription.

For more information please contact researchonline@ljmu.ac.uk

http://researchonline.ljmu.ac.uk/

Ocean Engineering 338 (2025) 122005

Contents lists available at ScienceDirect

Ocean Engineering

journal homepage: www.elsevier.com/locate/oceaneng

Research paper

Bending behaviour of rigid-flexible combined inflatable membrane structures for floating bridge modules

Yunling Ye [a,b], Jin Gan [a,b], Huabing Liu [c], Weiguo Wu [c], Lin Wang [d,e,*], Junyu Guo [d,e], He Li [f,**]

[a] Key Laboratory of High Performance Ship Technology (Wuhan University of Technology), Ministry of Education, Wuhan, 430063, China
[b] School of Naval Architecture, Ocean and Energy Power Engineering, Wuhan University of Technology, Wuhan, 430063, China
[c] Green & Smart River-Sea-Going Ship Cruise and Yacht Research Center, Wuhan University of Technology, Wuhan, 430063, China
[d] School of Mechatronic Engineering, Southwest Petroleum University, Chengdu, 610500, China
[e] Oil and Gas Equipment Technology, Sharing and Service Platform of Sichuan Province, Chengdu, 610500, China
[f] Centre for Marine Technology and Ocean Engineering (CENTEC), Instituto Superior Técnico, Universidade de Lisboa, Lisbon, Portugal

ARTICLE INFO

Keywords:
Floating bridge
Inflatable membrane
Bending stiffness
Failure modes

ABSTRACT

This paper investigates the load-bearing characteristics of rigid-flexible combined inflatable floating bridge modules. A simplified numerical model incorporating air-membrane coupling is first developed and validated by experimental data. Accordingly, a numerical method is subsequently employed to analyse the structural behaviour of the floating bridge module, including load-deformation feature, failure modes, and the effects of key structural parameters on the structural behaviour. The results reveal an initial linear load-deformation followed by softening, leading to local buckling failures. The parametric study indicates that an increased deck plate thickness, deck height, and internal pressure effectively enhance the load-bearing capacity of the floating bridge module. An equivalent stiffness prediction model is constructed with a prediction error of 0.594 % against numerical results. Overall, this study advances the understanding of load-bearing characteristics for inflated rigid-flexible combined floating bridge modules.

1. Introduction

Portable and deployable floating bridges play a critical role in disaster relief by rapidly restoring access to essential resources and services in affected areas. To date, innovative inflatable floating structures have emerged as promising solutions for temporary bridging and marine engineering applications (Russell and Thrall, 2013; Li et al., 2025). For instance, the Lightweight Modular Causeway System (LMCS), in Fig. 1 (a), demonstrates remarkable load-carrying capacities and reduces over 50 % mass over steel-truss-based structures. The inflatable bladders improve efficiency in storage, transportation and rapid deployment. These features make the inflatable structure an ideal solution for addressing the logistical challenges associated with temporary causeways in disaster relief operations. Even though incorporating inflatable membrane structures into floating bridge designs effectively reduces self-weight, the transverse arrangement of bladders limits their load-bearing capacity, requiring an overly heavy deck design to compensate. To address these limitations, it is necessary to create an improved floating bridge design of rigid-flexible combined pontoon (RFCP), see Fig. 1 (b), where inflatable bladders are arranged longitudinally instead of transversely, which enhances the load-bearing capacity and achieves greater structural lightweight.

The novel inflatable floating bridge modules offer advantages such as lightweight construction, compact storage, and easy-to-operate (Turner et al., 2008). Nevertheless, the nonlinear behaviour of inflatable composite membranes and the complex interactions between the deck and membrane pose challenges in the design process (Ye et al., 2025). These complexities are further heightened when considering bending behaviour and failure processes, driven by the pressure-dependent properties of the membranes (Wang et al., 2020). As a result, understanding the bending capacity of these modules becomes essential for optimising the designs and expanding applications.

Inflatable membrane structures, which serve as key components of inflatable floating bridges, take the form of tubes or beams and function

* Corresponding author. School of Mechatronic Engineering, Southwest Petroleum University, Chengdu, 610500, China.
** Corresponding author.
E-mail addresses: lincw_wang@qq.com (L. Wang), he.li@centec.tecnico.ulisboa.pt (H. Li).

https://doi.org/10.1016/j.oceaneng.2025.122005
Received 29 April 2025; Received in revised form 10 June 2025; Accepted 22 June 2025
Available online 30 June 2025
0029-8018/© 2025 The Authors. Published by Elsevier Ltd. This is an open access article under the CC BY license (http://creativecommons.org/licenses/by/4.0/).

as flexural elements in engineering applications (Liu et al., 2019, 2023; Cao et al., 2018). To simplify the structural analysis, they are often idealised as "beams", with studies focusing on their bending behaviour. For instance, Wielgosz and Thomas (Wielgosz and Thomas, 2002; Thomas and Wielgosz, 2004) employed Timoshenko beam theory and as a basis of that to construct a finite element (FE) model, treating internal pressure as a follower force. Similarly, Apedo et al. (2010) predicted load-deflection behaviour of the inflatable beam by using the virtual work principle, the model was then improved by incorporating pre-stress equations so as to account for the influence of internal pressure (Nguyen et al., 2015). Further developments also include the modelling of wrinkling loads with consideration of the impact of initial pressure and diameter (Elsabbagh, 2015).

On the other hand, the structural failure of inflatable membranes is typically characterised by localised wrinkling, which appears as small, localised surface folds, and arises from changes in membrane tension or shape (Ji et al., 2017; Martins et al., 2020). For instance, Stein and Hedgepeth (1961) introduced the "true membrane" model to estimate wrinkle loads based on the assumption that compressive stresses are not permissible. The results indicate that wrinkle and collapse loads are the results of internal pressure and cross-sectional dimensions (Haughton and McKay, 1996). Further investigations also engaged in the wrinkle loads of inflatable membrane structures under high internal pressure (Le van and Wielgosz, 2005; Apedo et al., 2009). Nevertheless, predicted failure loads are underestimated due to the neglect of membrane stiffness. To address this limitation, the shell model is introduced to predict wrinkle loads utilising the shell's critical buckling load (Veldman, 2006). However, both the membrane and shell models represent idealised conditions that deviate from experimental results. Thus, the concept of a "wrinkling factor" is proposed, which integrates both the membrane and shell models to achieve better consistency with experimental wrinkling load results (Wang et al., 2010, 2012).

Inflated membrane structures are valued for their high strength-to-weight ratio. However, the poor compressive capacity restricts their development in ocean engineering. To this end, rigid-flexible combined structures are developed, which are designed to utilise the compressive strengths of rigid structures and the tensile strengths of inflated membrane structures. Luchsinger et al. (2011) proposed a new design of spindle-shaped Tensairity girder system integrating struts, tensioned cables and inflated beams. Their research employed simulations and experimental testing to analyse the structural behaviour of the novel structure under bending, revealing that internal air pressure significantly affects the structural stiffness (Galliot and Luchsinger, 2013). Catarci et al. (2024) improved the structure by introducing NiTiNOL cables and evaluated their durability under cyclic loading. Moreover, research extended the rigid–flexible concept to complex geometries, such as the Tensairity dome developed by Wan et al., 2018, 2021, with its structural performance evaluated under various external loading conditions. Roekens et al. (2016) focused on optimising arch configurations and concluded that the inflatable rigid-flexible combined arch exhibits greater load-bearing capacity compared to the conventional inflatable arch system. These findings highlight the potential of inflatable rigid-flexible combined structures as an innovative ocean engineering sector.

It is pointed out that: (i) Most investigations above simplifies internal gas pressure as a uniform load, neglects the complex gas-membrane coupling effects, which, however, become critical for structural behaviour prediction; (ii) Existing studies explored bending behaviours of inflatable structures and rigid–flexible combined structures, but comprehensive parametric analyses to quantify the influence of the key factors are still not available; (iii) The absents of predictive models for equivalent stiffness limits applications of these structures in inflatable floating bridges. To this end, this study proposes a novel analysis of inflated membrane structures in floating bridges. A numerical model considering the gas-membrane coupling is developed and verified through experimental comparisons. The developed numerical model is then employed to analyse the inflatable floating bridge modules' bending and failure behaviour. A parametric study is conducted to explore the effect of deck and membrane stiffness on the structural characteristics of the inflatable floating bridge modules. Finally, an empirical formula for equivalent stiffness is proposed and optimised using analysis of variance (ANOVA). The novel contributions of this study are as follows:

(1) Develop a numerical model considering gas-membrane coupling effects based on the fluid cavity method.
(2) Conduct a parametric model to analyse the effects of critical parameters on structural behaviours of the inflatable floating bridge modules.
(3) Investigate a predictive formula for the equivalent stiffness of inflatable floating bridge modules.

The remainder of this paper is organised as follows. In Section 2, a simplified numerical model considering air-membrane interaction is developed and verified by experimental data. Section 3 analyses the load-deflection response and failure behaviour of floating bridge modules. Section 4 conducts a parametric study to evaluate the influence of deck height, deck plate thickness and internal pressure on the load-bearing capacity of floating bridge modules. An empirical formula of equivalent stiffness is developed, with regression parameters optimised through ANOVA. The conclusions are drawn in the end.

2. Numerical model and experimental verification

2.1. Simplified numerical models and experimental tests

Accurate numerical modelling is essential for analysing the mechanical behaviour of inflatable rigid-flexible floating bridge modules. The model should account for directional-dependent material properties of the composite membranes, the coupling effect between internal gas and membrane, and the non-convergence issues from rigid-flexible contact. Therefore, a simplified numerical model is developed using

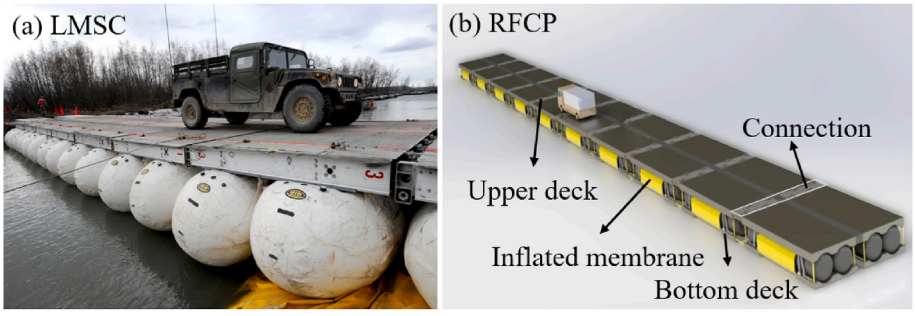

Fig. 1. New-type inflatable floating bridges: (a) Lightweight Modular Causeway System (LMCS); (b) Rigid-Flexible Combined Pontoon (RFCP).

explicit dynamic theory in ABAQUS, and an experimental setup is designed to validate the accuracy and reliability of the proposed model. This study focuses on the structural response of the inflated membrane and deck system without considering the surrounding water.

Fig. 2 shows the simplified numerical model of a 4 m rigid-flexible structure, consisting of a 150 mm wide deck with adjustable heights of 20 or 30 mm, and a cylindrical inflatable membrane with a 400 mm diameter. The internal pressure varies from 30 to 70 kPa with an interval of 10 kPa. Mechanical interactions between the deck, membrane and supports are modelled using the penalty function method. Boundary conditions simulate simple supports by constraining all degrees of freedom except the left support's X-axis displacement and both supports' Y-axis rotations. Quasi-static loading is applied through reference points, which are connected to the corresponding structural nodes using multi-point constraints (MPCs).

The material properties of the inflatable membrane are represented using an orthotropic constitutive model such that to account for the mutually orthogonal woven yarns. Uniaxial tensile tests, conducted in accordance with ASTM D4851 (Standard Test Methods for Coated, 2019), provide four essential material parameters: Warp modulus $E_{12} = 1019$ MPa, weft modulus $E_{21} = 232$ MPa, shear modulus $G_{12} = 19.29$ MPa and Poisson's ratio $\upsilon_{21} = 0.81$. Moreover, the deck is modelled as an isotropic elastic-plastic material governed by the von Mises yield criterion, with a Young's modulus E of 69 GPa, a Poisson's ratio υ of 0.33, and a yield stress σ_y of 204 MPa. The model parameters are detailed in Table 1.

Traditional methods simplify internal gas pressure as uniform surface loading, which fails to capture the dynamic interaction between the internal gas and the deformable membrane during structural deformation. To address this limitation, a coupled gas-membrane interaction model is developed using the fluid cavity method. This method determines the internal pressure based on the volume of the fluid cavity. The coupling between internal pressure and structural deformation is realised through volume changes induced by structural deformation. As Fig. 3 shows, the element includes wall nodes attached to the membrane surface and a reference node that governs internal pressure based on real-time volume tracking. The internal pressure is calculated according to the ideal gas law ($PV = nRT$), where P is the absolute pressure, V is the gas volume, n is the number of moles of gas, R is the gas constant, and T is the absolute temperature. The term of nRT is constant in the loading process, enabling accurate simulation of pressure-volume coupling during deformation. Pressure application and volume monitoring are integrated through the reference node, where structural deformation-induced changes in cavity volume automatically update the internal pressure. With this closed-loop feedback mechanism, gas pressure

Table 1
Model parameters of the rigid-flexible structure.

Component	Parameter	Value/Description
Membrane	Length	4000 mm
	Diameter	400 mm
	Internal pressure	30–70 kPa (10 kPa interval)
	Material	Orthotropic woven fabric
	$E_{12}/E_{21}/G_{12}/\upsilon_{21}$	1019 MPa/232 MPa/19.29 MPa/0.81
Deck	Length	4000 mm
	Width × Height	150 mm × 20/30 mm
	Material	Isotropic elastic-plastic
	$E/\sigma_y/\upsilon$	69 GPa/204 MPa/0.33
Boundary	Support type	Simple supports
Interface	Contact model	Penalty function
Loading	Method	Quasi-static via reference points using MPCs

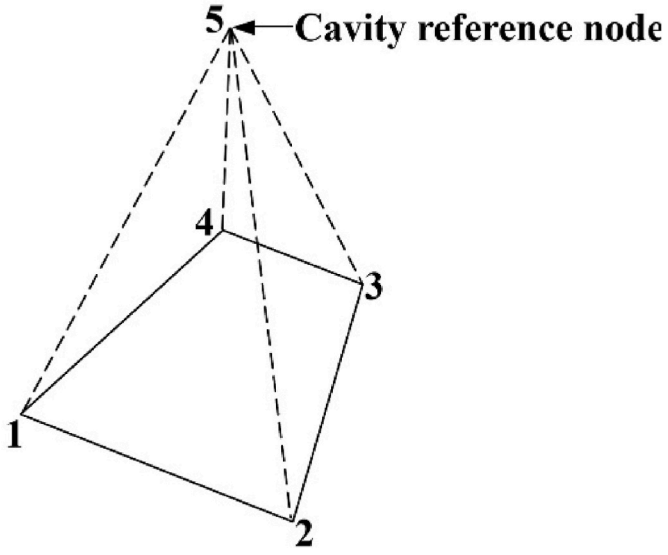

Fig. 3. Schematic diagram of the 4-node fluid volume element.

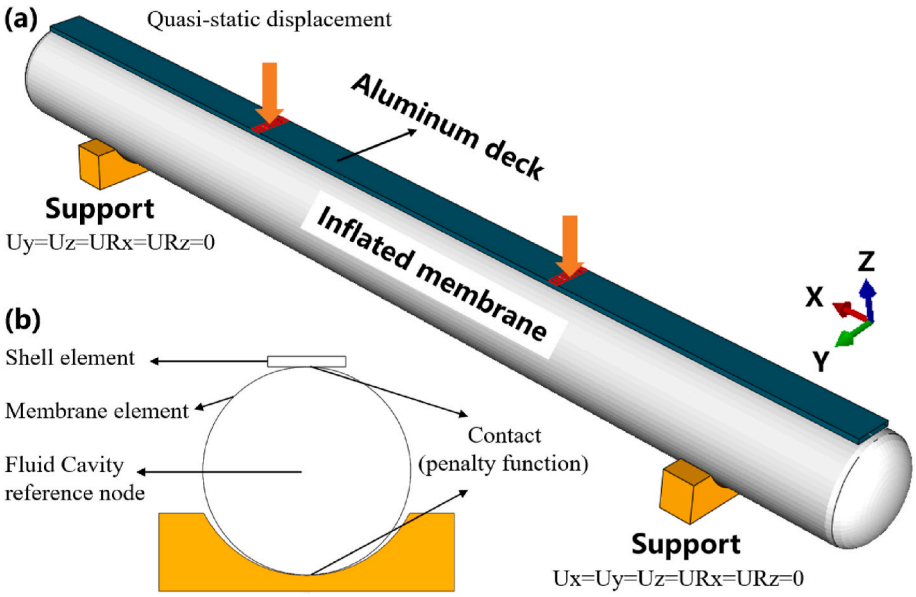

Fig. 2. Numerical model of the rigid-flexible combined structure: (a) Geometric model and Boundary conditions; (b) Elements and contact.

effects can be precisely simulated during both inflating and loading conditions.

Fig. 4 illustrates the experimental specimen, matching the numerical model dimensions. Inelastic belts bind the deck and membrane. Wooden supports with wheels provide simply supported boundary conditions. Static loading is applied through an electric jackscrew and distributed uniformly via a spreader beam and I-beam assembly. Deformation is measured using six linear variable differential transformers (LVDTs), and the applied load is measured by an S-type load cell. Internal pressure is monitored with a pressure gauge. Note that the experimental pressure range is limited to 70 kPa to ensure test safety during the loading process.

2.2. Numerical modelling verification

Fig. 5 presents a typical deformed state with a deck height of 30 mm under 60 kPa internal pressure. The overall deformation from the numerical model matches the experimental observations. During the initial loading stage, the deck and inflated membrane deform in coordination. With increasing load, localised depressions form at the deck's loading points, which leads to a total deformed pattern change to trilinear as Fig. 5 (a). The local buckling would not immediately lead to structural failure due to the support provided by the inflated membrane. However, as the applied load increases, the buckling-induced degradation of structural stiffness accumulates, and the structure reaches its maximum bending capacity. Fig. 5 (b) illustrates the local failure mode. A depression forms on the deck's top near the loading point, followed by a bulge on the adjacent lateral face as the load increases. With its vertical developing, the local structural integrity weakens progressively at the loading points, ultimately resulting in a complete loss of structural load-bearing capacity.

The numerical and experimental mid-span load-deformation curves are illustrated in Fig. 6 (a). They demonstrate close agreement throughout the loading process, exhibiting an initial linear phase succeeded by a progressive softening behaviour. Equivalent structural stiffness is quantified through linear fitting of the load-deformation data within the elastic phase. As illustrated in Fig. 6 (b), comparisons under varying internal pressures (30–70 kPa) and deck heights (20 or 30 mm) reveal good consistency between numerical and experimental values. This validation confirms that the developed numerical model achieves a high-precision representation of the inflatable structure's mechanical response.

3. Numerical analysis of rigid-flexible combined floating bridge modules

3.1. Numerical model

A numerical model of the rigid-flexible combined structure is developed and the superiority of the numerical model is verified by comparing it with the experimental test. Then, the developed numerical model is employed to analyse the bending behaviours of the rigid-flexible combined floating bridge module. As Fig. 7 shows, the geometric model of the rigid-flexible combined floating bridge module is assembled of the upper deck, inflated membrane and bottom deck. The deck is a stiffened panel which consists of two plates, five transverse stiffeners and longitudinal stiffeners. The geometric dimensions refer to a practical floating bridge. The specific parameters are as follows: The length of the module is $l = 8000$ mm, while the width of the deck is $b = 4000$ mm and the diameter of the inflated membrane is $r = 1600$ mm. The thickness of the deck and the membrane are $t_d = 1$ mm and $t_m = 0.68$ mm, respectively. Furthermore, to comprehensively assess the influence of internal pressure on the structural behaviour, the pressure range is extended up to 120 kPa.

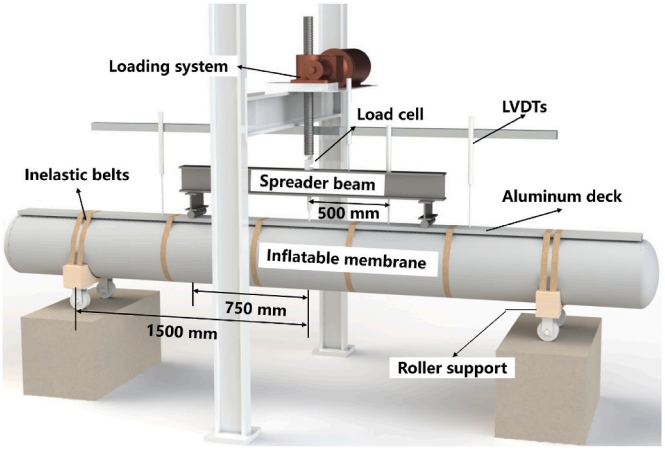

Fig. 4. Experimental configuration of the rigid-flexible combined structure.

The material properties of the membrane are defined in the same way as the numerical model in Section 2. An elastic-perfectly plastic material model is employed to define the deck's material properties in which the Young's modulus is 69 GPa, Poisson's ratio of 0.33 and the yield stress is 204 MPa. The membrane's material properties are defined by an orthotropic model with Young's modulus E_{12} of 1019 MPa, E_{21} of 232 MPa, Shear modulus G_{12} of 19.29 MPa and Poisson's ratio of 0.81.

To simulate the simple boundary conditions, the nodes of the deck's ends are constrained, with only the y-displacement and z-rotation being free. Quasi-static deformations are applied at the nodes along the loading positions of the deck to produce the bending moment. Contact between the deck and inflated membrane is established using the penalty function method.

The deck and inflated membrane are generated using S4R shell elements and M3D4R membrane elements, respectively. Fig. 8 illustrates the mesh convergence curves through refinement from 150 to 50 mm element sizes with 25 mm decrements. The deformation patterns, equivalent stiffness and ultimate load change exhibit asymptotic convergence when the element size reaches 75 mm. Thus, the selected 75 mm element size is sufficient to capture the global and local deformation behaviours of the deck and inflatable membrane accurately.

3.2. Load-deformation response and failure mode

The numerical model demonstrates two typical deflected states during the loading process. During the initial loading phase, as detailed in Fig. 9 (a), the overall deformation is minimal and is primarily concentrated in the upper deck, while the other components remain nearly undeformed. As the load increases, plastic deformation begins to appear in the loading area of the upper deck, as illustrated in Fig. 9 (b), and the overall deformation increases. The deflection curve exhibits a trilinear shape, with the loading point serving as the inflexion point, and the middle segment of the deformed model forming a straight line.

The load-deformation curves of the mid-span points under varied internal pressures are plotted in Fig. 10 (a). The curves exhibit an initial linear behaviour followed by softening. As the internal pressure increases, the slope and maximum load of the curves increase. Additionally, in order to analyse the failure behaviour of the model, a typical internal pressure result at 100 kPa is shown in Fig. 10 (b). In the initial loading stage (OA), the curves show a linear characteristic, and the numerical models stay in the elastic stage, with all the structural components undergoing elastic deformation. As the load exceeds point A, plastic deformation begins to appear in the upper deck, then local buckling occurs in the loading regions of the upper deck. In the nonlinear AB segment, the upper deck fails due to the accumulation of local plastic deformation. The structure then enters the post-buckling stage (BC), during which the load is carried by the inflated membrane and the bottom deck. In this stage, a slight increase in load results in a significant increment in deformation. Ultimately, the bottom deck fails, corresponding to the ultimate state at point C. The model has completely failed at this point.

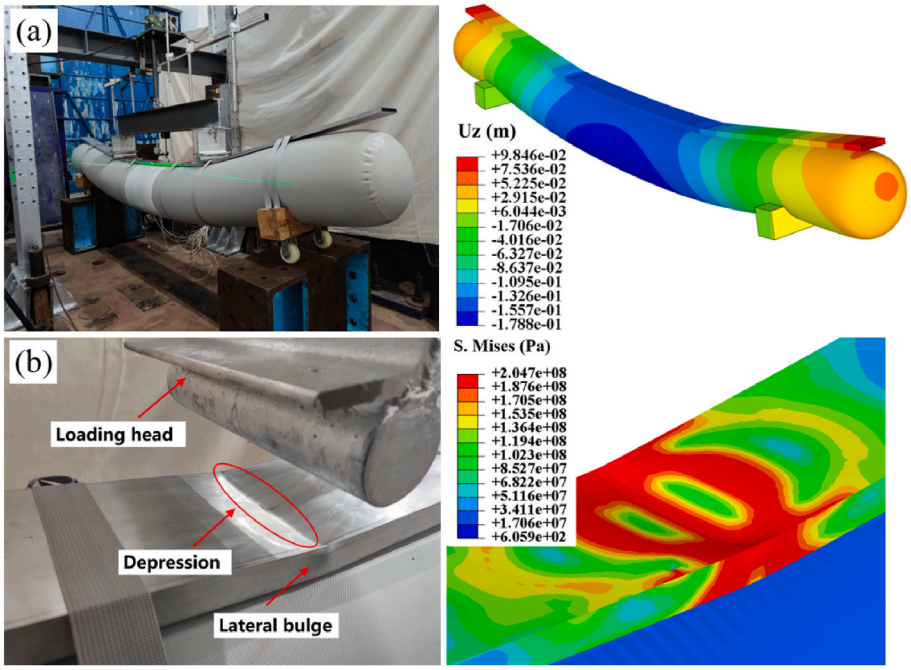

Fig. 5. Typical deformed states of the 60 kPa specimen: (a) Global deformed pattern; (b) Local structural failure.

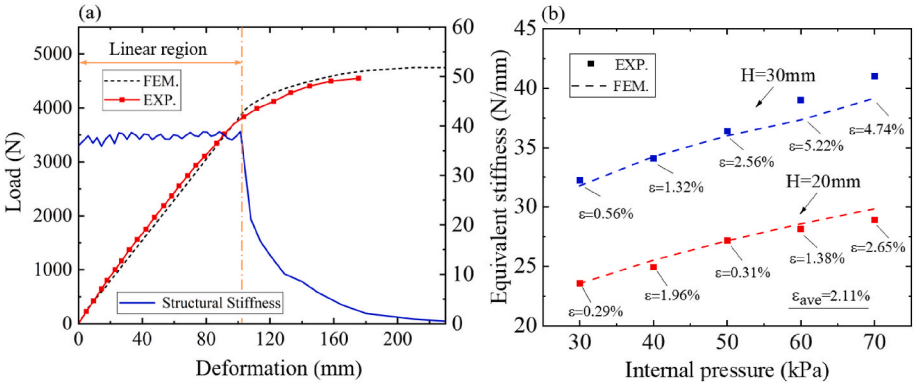

Fig. 6. Numerical and experimental comparison for the mid-span load-deformation response: (a) Load-deformation curves; (b) Equivalent stiffness within the linear stage.

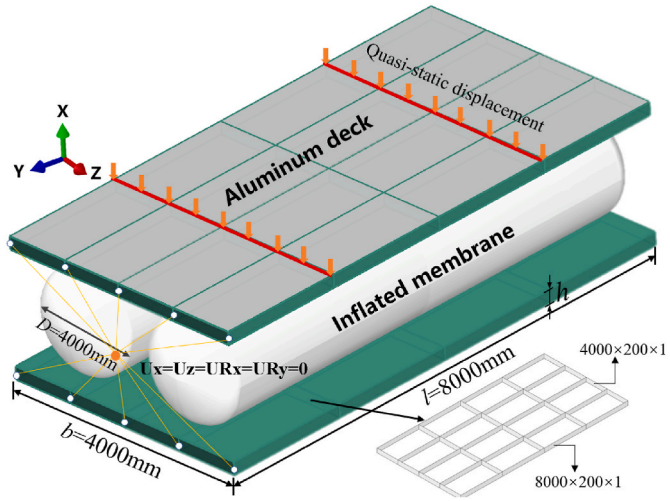

Fig. 7. Numerical model of the rigid-flexible combined floating bridge module.

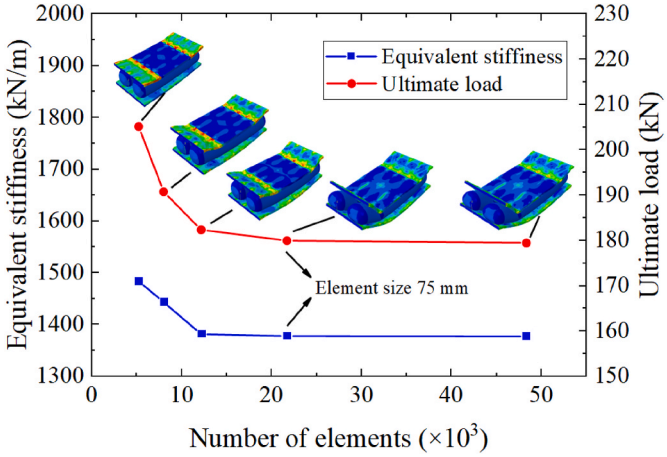

Fig. 8. Mesh convergence curves.

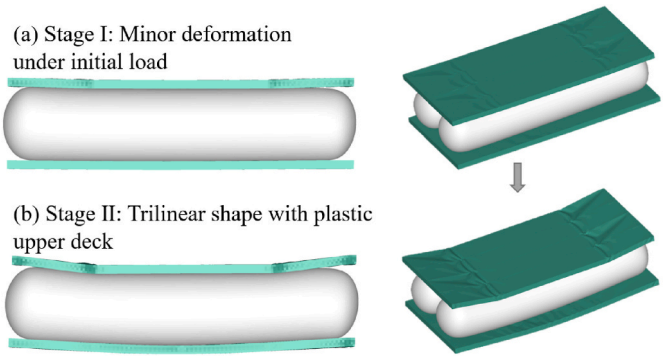

Fig. 9. Typical deformed models: (a) Under initial load; (b) Close to ultimate load.

Table 2
Parametric study cases.

Case	FE model	Internal pressure p (kPa)	Deck height h (mm)	Deck thickness t (mm)
1–10	Pontoon		180	
11–21	module		185	
22–32			190	
33–43			195	
44–54		20-120 (interval 10)	200	0.8-1.2 (interval 0.1)
55–65			205	
66–76			210	
77–84		80	200	0.5- 4(interval 0.5)
85–89				
90–131	Deck	/	180-210 (interval 5)	0.7- 1.2 (interval 0.1)
132–142	Inflated membrane	20-120 (interval 10)	/	/

4. Parametric study

4.1. Scheme of the parametric study

A comprehensive parametric study is performed using the developed numerical model to investigate the influence of the deck's plate thickness, deck height and internal pressure on the bending characteristics of the rigid-flexible combined floating bridge module. The dimensions of the structural components of the floating bridge modules used in the parametric analyses are specified in Table 2. A total of 142 FE models, consisting of 89 floating bridge modules and 53 components, are created out of the parametric analyses. The 53 component models are specifically utilised to derive the equivalent stiffness of the deck (k_1) and the inflated membrane (k_2). The k_1 and k_2 are then used to analyse the effects of deck's plate thickness, deck height and internal pressure on the bending characteristics of the rigid-flexible combined floating bridge module.

The results of the component models (cases 90–142) are shown in Fig. 11. The equivalent stiffness of the deck k_1 shows a linear relationship with the deck height and thickness, while the equivalent stiffness of the inflated membrane k_2 also exhibits a linear increase with rising internal pressure.

4.2. Effect of deck's height and plate thickness

The effects of deck stiffness k_1 on the stiffness of floating bridge modules are shown in Fig. 12. Here, k_1^t and k_1^h represent the effects of deck plate thickness and deck height, respectively. As the k_1^t and k_1^h increase, the stiffness of floating bridge modules increases, with an almost linear relationship observed across all internal pressures. Additionally, Fig. 10 shows the linear relationship between deck stiffness and both deck plate thickness and height. Thus, it suggests that these structural parameters have a directly proportional influence on the stiffness of the floating bridge modules. Moreover, the curves of Fig. 12 (a) and (b) are linearly fitted and the slopes of the linear fit curves are presented in Fig. 12 (c). The slopes for k_1^t curves are higher than those for k_1^h curves, indicating the equivalent stiffness is more sensitive to deck plate thickness. However, the slope does not consistently increase or decrease with internal pressure. This irregular trend indicates a more complex interaction between internal pressure and deck dimensions.

As shown in Fig. 13, the load-deformation response mode of the modules varies with different plate thicknesses. Under the initial load, the deformed patterns of the modules are similar, characterising minor overall deformation. However, with increased loading, significant differences emerged in failure modes, such as the plate thickness $t = 4$, the decks and the inflated membrane experience simultaneous failure. In contrast, with a plate thickness of $t = 0.7$ mm, the module exhibits a progressive failure process. As the load increases, the upper deck fails, then the load is transferred through the inflated membrane to the lower deck until it fails, leading to the complete structural failure.

Analysing the numerical results of all 89 cases, the stiffness of the deck and the inflated membrane significantly influence the failure mode of modules. When the inflated membrane's stiffness is close to or greater than the deck's stiffness, the module experiences simultaneous failure. When the inflated membrane's stiffness is significantly lower than the deck's stiffness, the module shows a progressive failure mode. Thus, the inflated membrane-deck stiffness ratio β is defined, and its relationship with failure mode is shown in Table 3. It can be found that 0.55 is a threshold; when $0 < \beta \leq 0.55$ the module experiences simultaneous failure, whereas for $\beta > 0.55$ the module undergoes progressive failure.

4.3. Effect of internal pressure

As shown in Fig. 14 (a), the stress distribution under inflation is generally consistent throughout the inflated membrane (except near the ends of the model where stress gradients occur due to geometric changes, which are beyond the scope of this study). This behaviour

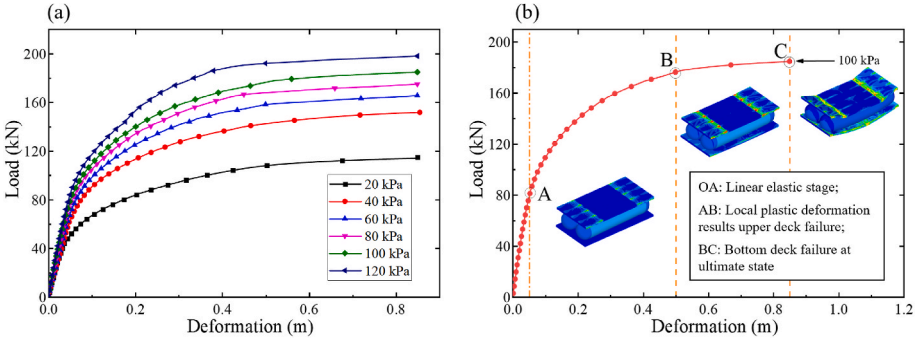

Fig. 10. (a) Mid-span load-deformation relationship and (b) structural failure process.

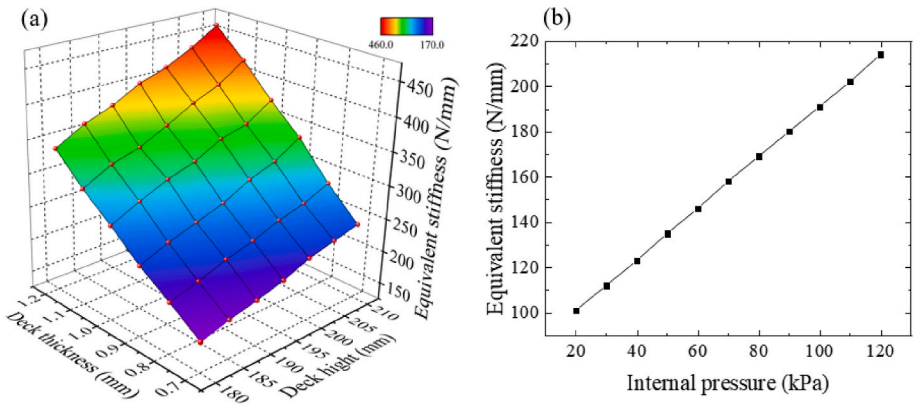

Fig. 11. The equivalent stiffness of the deck (a) and the inflated membrane (b).

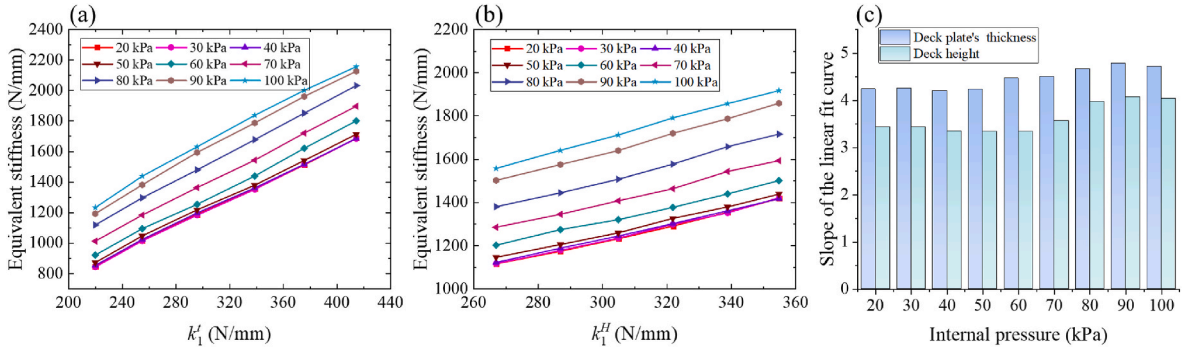

Fig. 12. The effect of deck stiffness: (a) The effect of deck plate thickness; (b) The effect of deck height; (c) Slops of the linear fit curves.

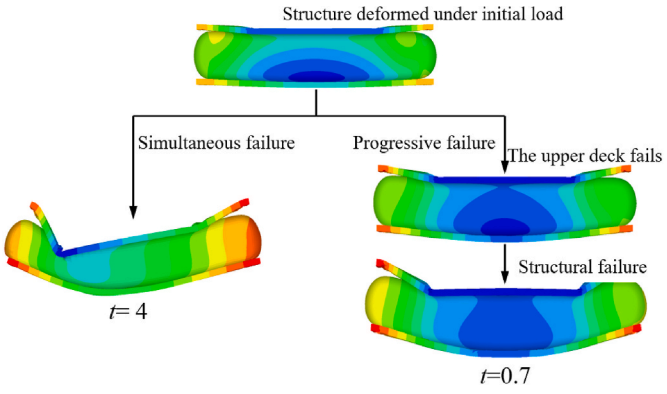

Fig. 13. Load-deformation response with varied deck plate thickness.

Table 3
The relationship between β and failure mode.

Stiffness ratio	Failure mode
$0 < \beta \leq 0.55$	Simultaneous failure
$\beta > 0.55$	Progressive failure

matches the theoretical stress distribution pattern (Nguyen et al., 2015; Ji et al., 2017).

In the numerical model, the fluid cavity method is employed to simulate internal pressure, which enables an accurate representation of the interaction between internal gas and the membrane. As illustrated in Fig. 14 (b), deformation of the inflated membrane under external loads leads to a reduction in the volume of the inner cavity. Since the amount of gas remains constant, which means the product of pressure and volume (*PV*) remains unchanged, the internal pressure would increase accordingly. Notably, this pressure variation becomes significant during the nonlinear deformation phase (Ye et al., 2023, 2024). Therefore, the variation in internal pressure cannot be ignored and the developed numerical model effectively captures this structural behaviour.

The internal pressure has a significant influence on the failure mode of the inflatable floating bridge module. With the increase in internal pressure, it is observed that the failure mode of the numerical model changes. For example, when the internal pressure is 20 kPa (with a stiffness ratio β of 0.3), the numerical model shows simultaneous structural failure; whereas when the internal pressure increases to 100 kPa (with a stiffness ratio β of 0.56), the failure mode changes to be progressive. These results confirm the influence of stiffness ratio on failure mode, as summarised in Table 3.

To investigate the effect of internal pressure on the equivalent stiffness of the floating bridge module (k_m), numerical analyses are conducted for deck heights of 200 mm, 205 mm, and 210 mm, with internal pressures ranging from 10 to 120 kPa. Fig. 15 shows that the equivalent bending stiffness k_m increases as the internal pressure increases for all deck height cases. However, unlike the linear effect of deck stiffness (k_1), the effect of inflated membrane stiffness (k_2) on k_m exhibits an initial slow increase, followed by a rapid rise, and then a gradual decrease in the rate. For instance, at internal pressures below approximately 60 kPa (denoted as region A), the variation in stiffness values across all configurations remains minor. As the internal pressure exceeds 60 kPa, a noticeable rise in stiffness is observed. Nonetheless, beyond approximately 90 kPa (Region B), the increase rate in equivalent bending stiffness gradually diminishes. Thus, increasing the internal pressure effectively enhances the load-bearing capacity of the module, however, the benefits show diminishing returns at higher pressure levels. Moreover, higher internal pressures impose greater demands on the manufacturing precision and material performance of the membrane

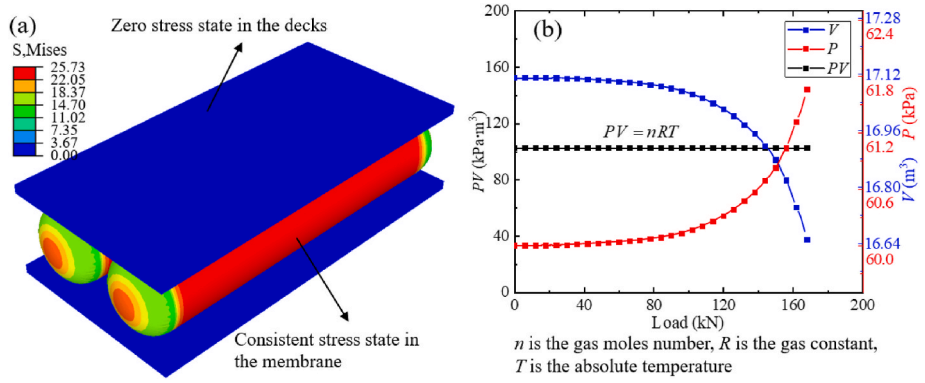

Fig. 14. (a) The deformation nephogram under inflation; (b) Internal pressure and volume cavity under loading.

structure. Within the scope of this study, the optimal internal pressure is approximately 90 kPa.

4.4. Empirical formula of equivalent stiffness

To develop an empirical formula of equivalent stiffness, a cubic response surface model is constructed using multiple linear regression. This model incorporates $k = 3$ regressor variables: X_1 (the plate thickness t), X_2 (the deck height H) and X_3 (the internal pressure p). The relationship is expressed as:

$$F(X_j) = \beta_0 + \sum_{j=1}^{3}\beta_j X_j + \sum_{j=1}^{3}\beta_{jj}X_j^2 + \sum_{j=1}^{3}\beta_{jjj}X_j^3 + \sum\sum_{i<j=2}^{3}\beta_{ij}X_iX_j + \sum\sum_{i<j=2}^{3}\beta_{iij}X_i^2X_j + \sum\sum_{i<j=2}^{3}\beta_{iij}X_iX_j^2 + \beta_{123}X_1X_2X_3 \quad (1)$$

This equation includes terms for linear, quadratic, and cubic effects of individual variables, as well as interaction terms accounting for combined effects between variables. The regression coefficients β quantify the contribution of each term to the predicted equivalent stiffness.

To assess the contribution of each regressor variable and their interactions, a parametric analysis is conducted using a multiple linear model analysis of variance (ANOVA), further refined by the least-squares method (LSM). Based on the parametric analysis results, terms in Equation (1) with a p-value >0.01 are excluded from the unchanged final formula.

Table 4
Results of the equivalent stiffness from RSM and FEM.

Order	X_1: t (mm)	X_2: H (mm)	X_3: p (kPa)	k_m^{FEM} (N/mm)	k_m (N/mm)	Error (%)
1	0.8	195	20	976.56	983.32	0.69
2	0.8	210	20	1120.23	1127.64	0.66
3	0.8	205	20	1065.95	1077.68	1.10
4	0.8	200	20	1016.45	1029.48	1.28
…	…		…	…	…	…
277	1.1	195	110	2062.52	2068.21	0.28
278	1.1	200	110	2122.61	2139.20	0.78
279	1.1	205	110	2211.76	2206.80	−0.22
280	1.1	210	110	2269.14	2270.75	0.07

Using the developed numerical model, a total of 280 case studies are conducted to obtain the equivalent stiffness k_m of floating bridge modules. Selected results are summarised in Table 4.

The ANOVA results of the cubic model are presented in Appendix Table A. The Model F-value of 5.172×10^3 indicates that the model is significant, with only a 0.01 % probability that such a large F-value could occur due to noise. Moreover, in this case, X_1, X_2, X_3, X_1X_2, X_1X_3, X_2X_3, $X_3^2X_1$, $X_1X_2^2$, $X_1X_3^2$ and X_3^3 are significant model terms, as their p-values are less than 0.01. However, terms with p-values greater than 0.10, including X_2^2, $X_1X_2^2$, X_1^3, and X_2^3, are considered insignificant and excluded to refine the predictive model.

Appendix Table B summarises the reduced cubic (RC) model, which remains significant with a Model F-value of 9.412×10^3 and the p-values of all the terms below 0.001. Furthermore, the predicted R^2 value of

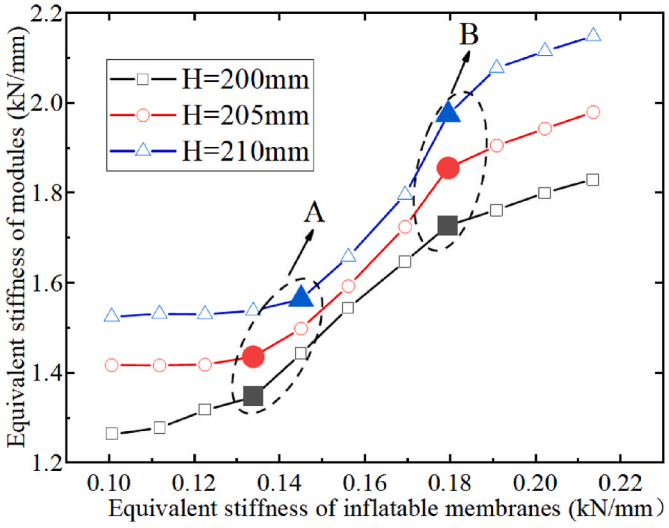

Fig. 15. The effect of inflated membrane stiffness with varied deck heights.

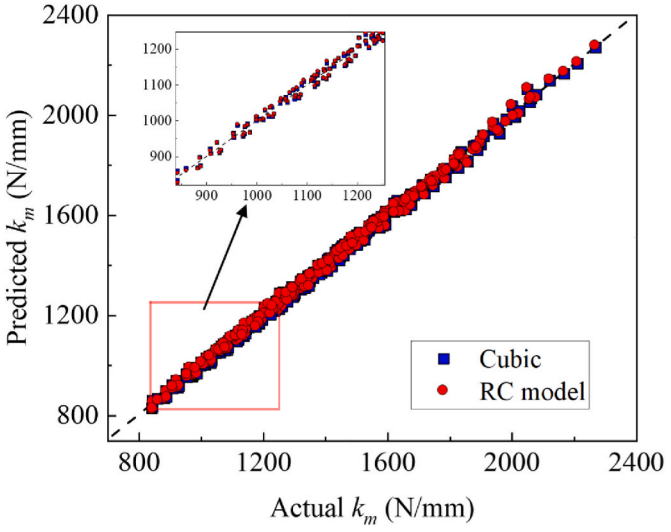

Fig. 16. Cubic and RC models' predictions for the k_m values.

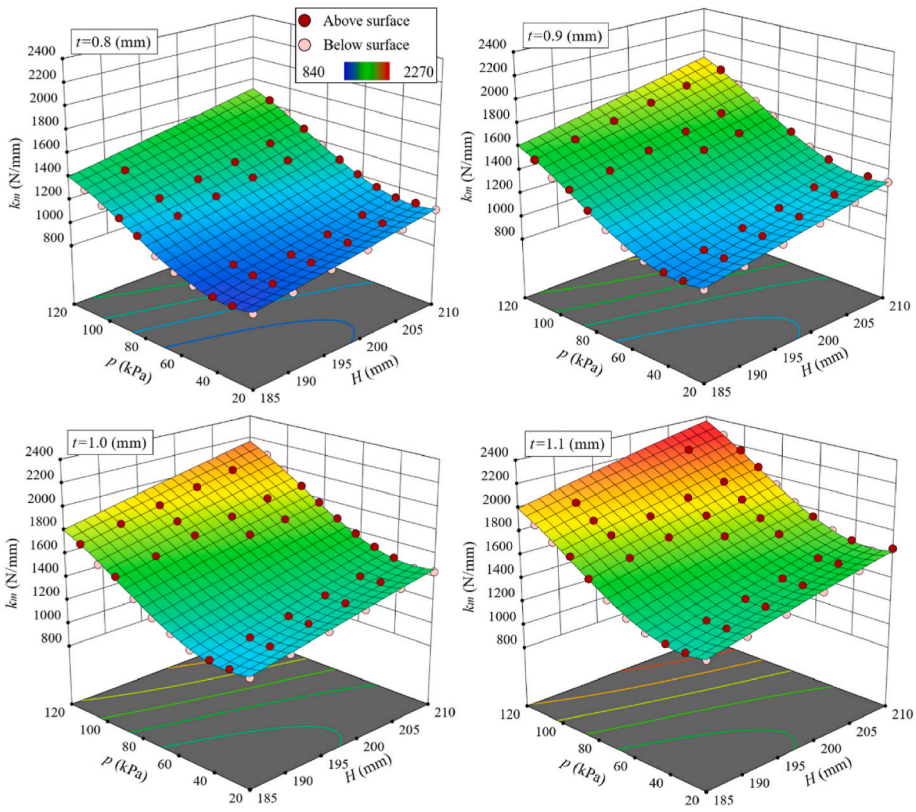

Fig. 17. Response surface of k_m for RC model.

0.9972 aligns closely with the Adjusted R^2 of 0.9970, both being close to 1. A signal-to-noise ratio of 446.07, far exceeding the threshold of 4. These parameters confirm the superiority of the RC model. The final formula for the equivalent stiffness $k_m(t, H, p)$ is denoted by the RC model,

$$k_m(t,H,p) = -94.62 - 987.06t + 0.0398H - 10.02p + 15.54tH - 1.58tp + 0.0253p^2 - 0.0123tH^2 + 0.0464tp^2 - 0.00107p^3 \quad (2)$$

where 0.8 mm $\leq t \leq$ 1.1 mm, 185 mm $\leq H \leq$ 210 mm and 20 kPa $\leq p \leq$ 120 kPa.

Predictions of k_m values from both the cubic and RC models are plotted in Fig. 16. All predicted points are close to the actual line, and the RC model shows no additional deviation compared to the full cubic model. Therefore, the RC model effectively represents the response surface for the equivalent stiffness $k_m(t, H, p)$.

Fig. 17 illustrates the response surface of the equivalent stiffness k_m based on the RC model. The three-dimensional response surface shows that the design points sit basically on the response surface, which indicates strong agreement between the predicted and FEM results. As shown in Table 4, the deviation values between the RC model and FEM are below 2 %, with an average of the deviation is 0.594 %, demonstrating high accuracy of the RC model. Therefore, the developed empirical formula provides a feasible alternative to the FEM for assessing the equivalent stiffness of the inflatable floating bridge modules within the investigated parameter range.

5. Conclusions

This study focuses on the rigid-flexible combined floating bridge module and investigates its load-bearing characteristics and equivalent bending stiffness by using a series of numerical simulations. The main conclusions are as follows:

(1) A numerical model considering air-membrane coupling effects is developed for the rigid-flexible combined structure and validated against experimental results. The numerical load-deformation relationship and failure modes match experimental results. The deviation of the equivalent stiffness keeps a minimal value with an average of 2.11 %.

(2) The deformation and failure modes of the floating bridge module are analysed. The load-deformation curves indicate an initial linear behaviour followed by softening. The deformation process confirms the curves' behaviour, which includes an initial elastic stage then transitions to local buckling, resulting in overall structural failure.

(3) The effects of deck plate thickness, deck height and internal pressure on the load-bearing capacity of the floating bridge module are investigated. Increasing the equivalent stiffness of either the inflated membrane or the deck enhances the load-bearing capacity of the floating bridge module. Deck stiffness exhibits a linear relationship with load capacity, while internal pressure shows an optimal range with the given deck stiffness.

(4) The stiffness ratio β, defined as the ratio between the deck stiffness and the inflated membrane stiffness, is introduced to analyse failure modes. When $0 < \beta \leq 0.55$, the structure exhibits simultaneous failure. As β exceeds 0.55, the failure mode transitions to progressive failure.

(5) An empirical formula for predicting the equivalent stiffness of the floating bridge module is developed. The significance of regression parameters is evaluated using ANOVA, and the model is optimised by removing insignificant terms. Comparison with numerical results shows an average error of only 0.594 %, indicating that the prediction formula is a feasible alternative to the numerical model.

This study focuses on the structural response of the floating bridge module under dry conditions, without considering the interaction with

the surrounding water. Such interaction could affect the global deformation and load-bearing behaviour of the inflatable floating bridge. Future work will incorporate fluid-structure interaction to improve the model's applicability to realistic marine environments.

CRediT authorship contribution statement

Yunling Ye: Writing – original draft, Methodology, Formal analysis. **Jin Gan:** Validation, Methodology, Data curation. **Huabing Liu:** Validation, Data curation. **Weiguo Wu:** Writing – review & editing, Supervision. **Lin Wang:** Methodology, Investigation, Formal analysis. **Junyu Guo:** Visualization, Validation, Methodology, Investigation, Formal analysis. **He Li:** Writing – original draft, Methodology, Formal analysis, Conceptualization.

Declaration of competing interest

This is no Conflict of Interests.

Acknowledgements

The authors acknowledge projects supported by Fundamental Research Funds for the Central Universities (WUT: 2022CG005 and WUT: 104972025RSCbs0184).

Appendix A. ANOVA Results Tables for Regression Models

Table A
ANOVA results of the cubic model.

Source	Sum of Squares	df	Mean Square	F-Value	p-Value
Regression	2.558×10^7	19	1.347×10^6	5.172×10^3	<0.0001
X_1	1.170×10^6	1	1.170×10^6	4.493×10^3	<0.0001
X_2	4.226×10^5	1	4.226×10^6	1.623×10^3	<0.0001
X_3	2.046×10^6	1	2.046×10^6	7.857×10^3	<0.0001
X_1X_2	1.594×10^4	1	1.593×10^4	61.23	<0.0001
X_1X_3	3.441×10^4	1	3.441×10^4	132.17	<0.0001
X_2X_3	1.128×10^4	1	1.128×10^4	43.34	<0.0001
X_1^2	458.69	1	458.69	1.76	0.1856
X_2^2	12.72	1	12.72	0.0489	0.8252
X_3^2	2.612×10^5	1	2.612×10^5	1.003×10^3	<0.0001
$X_1X_2X_3$	523.95	1	523.95	2.01	0.1572
$X_1^2X_2$	991.89	1	991.89	3.81	0.1520
$X_1^2X_3$	888.96	1	888.96	3.41	0.2658
$X_1X_2^2$	2.413×10^3	1	2.413×10^3	9.27	0.0026
$X_1X_3^2$	3.972×10^3	1	3.972×10^3	15.26	0.0001
$X_2^2X_3$	64.68	1	64.68	0.2484	0.6186
$X_2X_3^2$	740.18	1	740.18	2.84	0.1930
X_1^3	6.86	1	6.86	0.0264	0.8712
X_2^3	18.70	1	18.70	0.0718	0.7889
X_3^3	9.873×10^4	1	9.873×10^4	379.25	<0.0001
Residual	67,688	260	260.34		
R-squared	0.997				
Factor	Coefficient Estimate	Standard Error	95 % CI Low	95 % CI High	VIF
β_0-Intercept	1342.05	2.68	1336.78	1347.33	
β_1– t	357.11	5.33	346.62	367.60	9.54
β_2–H	145.05	3.60	137.96	152.14	8.92
β_3– p	441.51	4.98	431.70	451.31	8.80
β_{12}– tH	27.28	3.49	20.41	34.14	3.30
β_{13}– tp	54.24	4.72	44.95	63.53	3.04
β_{23}– Hp	17.96	2.73	12.58	23.33	1.85
β_{11}– t^2	−12.64	9.52	−31.38	6.11	13.71
β_{22}– H^2	0.5579	2.52	−4.41	5.53	2.81
β_{33}– p^2	134.87	4.26	126.49	143.26	1.90
β_{123}– tHp	−5.32	3.75	−12.72	2.07	1.31
β_{112}– t^2H	−9.41	4.82	−18.90	0.0830	4.64
β_{113}– t^2p	−12.41	6.71	−25.63	0.8142	4.57
β_{122}– tH^2	−9.48	3.11	−15.60	−3.35	3.11
β_{133}– tp^2	23.18	5.93	11.50	34.87	2.76
β_{233}–Hp^2	−1.51	3.03	−7.47	4.45	2.88
β_{111}– t^3	6.99	4.15	−1.17	15.16	2.60
β_{222}– H^3	−1.87	11.50	−24.51	20.78	27.78
β_{333}– p^3	−0.7270	2.71	−6.07	4.61	9.66

Table B
ANOVA results of the reduction-cubic model.

Source	Sum of Squares	df	Mean Square	F-Value	*p*-Value
Regression	2.558×10^7	19	2.558×10^6	9.412×10^3	<0.0001
X_1	3.250×10^6	1	3.250×10^6	1.196×10^4	<0.0001
X_2	3.007×10^6	1	3.007×10^6	1.106×10^4	<0.0001
X_3	2.669×10^6	1	2.669×10^6	9.820×10^3	<0.0001
X_1X_2	2.401×10^4	1	2.401×10^4	88.36	<0.0001
X_1X_3	6.021×10^4	1	6.021×10^4	221.55	<0.0001
X_2X_3	1.481×10^4	1	1.482×10^4	54.53	<0.0001
X_3^2	2.659×10^5	1	2.659×10^5	978.58	<0.0001
$X_1X_2^2$	2.448×10^3	1	2.448×10^3	9.01	0.0029
$X_1X_3^2$	3.972×10^3	1	3.972×10^3	14.62	0.0002
X_3^3	9.873×10^4	1	98,733	363.32	<0.0001
Residual	73,102	260	271.76		
R-squared	0.997				
Factor	Coefficient Estimate	Standard Error	95 % CI Low	95 % CI High	VIF
β_0-Intercept	1339.62	1.69	1336.29	1342.94	
β_1– t	349.14	3.19	342.85	355.42	3.28
β_2–H	143.68	1.37	140.99	146.37	1.23
β_3– p	436.95	4.41	428.27	445.63	6.61
β_{12}– tH	23.41	2.49	18.51	28.31	1.61
β_{13}– tp	49.10	3.30	42.61	55.60	1.42
β_{23}– Hp	15.83	2.14	11.61	20.05	1.09
β_{33}– p^2	133.47	4.27	125.07	141.87	1.83
β_{122}– tH^2	−8.71	2.90	−14.43	−3.00	2.59
β_{133}– tp^2	23.18	6.06	11.24	35.12	2.76
β_{333}– p^3	−133.56	7.01	−147.35	−119.76	7.72

References

Apedo, K.L., Ronel, S., Jacquelin, E., Massenzio, M., Bennani, A., 2009. Theoretical analysis of inflatable beams made from orthotropic fabric. Thin-Walled Struct. 47 (12), 1507–1522.

Apedo, K.L., Ronel, S., Jacquelin, E., Bennani, A., Massenzio, M., 2010. Nonlinear finite element analysis of inflatable beams made from orthotropic woven fabric. Int. J. Solid Struct. 47 (16), 2017–2033.

Cao, Z., Wan, Z., Yan, J., Fan, F., 2018. Static behaviour and simplified design method of a Tensairity truss with a spindle-shaped airbeam. J. Constr. Steel Res. 145, 244–253.

Catarci, S., Guruva, S.K., Carboni, B., Quaranta, G., Lacarbonara, W., 2024. Experimental nonlinear response of a new tensairity structure under cyclic loading. Thin-Walled Struct., 112163

Elsabbagh, A., 2015. Nonlinear finite element model for the analysis of axisymmetric inflatable beams. Thin-Walled Struct. 96, 307–313.

Galliot, C., Luchsinger, R.H., 2013. Structural behavior of symmetric spindle-shaped Tensairity girders with reinforced chord coupling. Eng. Struct. 56, 407–416.

Haughton, D., McKay, B., 1996. Wrinkling of inflated elastic cylindrical membranes under flexure. Int. J. Eng. Sci. 34 (13), 1531–1550.

Ji, Q., Wang, C., Tan, H., 2017. Multi-scale wrinkling analysis of the inflated beam under bending. Int. J. Mech. Sci. 126, 1–11.

Le van, A., Wielgosz, C., 2005. Bending and buckling of inflatable beams: some new theoretical results. Thin-Walled Struct. 43 (8), 1166–1187.

Li, H., Ding, Y., Sun, Y., Xie, M., Guedes Soares, C., 2025. An intelligent failure feature learning method for failure and maintenance data management of wind turbines. Reliab. Eng. Syst. Saf. 261, 111113.

Liu, Y., Zhang, D., Hu, J., Chen, W., Gao, C., Qiu, Z., 2019. Design and structural analysis of an inflatable coated fabric manipulation arm. Thin-Walled Struct. 139, 310–320.

Liu, P., Yue, M., Feng, S.Z., Ngamkhanong, C., 2023. Structural behaviour of air-inflated beams. Structures 47, 1613–1623.

Luchsinger, R.H., Sydow, A., Crettol, R., 2011. Structural behavior of asymmetric spindle-shaped Tensairity girders under bending loads. Thin-Walled Struct. 49 (9), 1045–1053.

Martins, A.D., Silvestre, N., Bebiano, R., 2020. A new modal theory for wrinkling analysis of stretched membranes. Int. J. Mech. Sci. 175, 105519.

Nguyen, Q.T., Thomas, J.C., Le van, A., 2015. Inflation and bending of an orthotropic inflatable beam. Thin-Walled Struct. 88, 129–144.

Roekens, J., De Laet, L., Mollaert, M., Luchsinger, R., 2016. Experimental and numerical investigation of a tensairity arch. Thin-Walled Struct. 105, 112–120.

Russell, B.R., Thrall, A.P., 2013. Portable and rapidly deployable bridges: historical perspective and recent Technology developments. J. Bridge Eng. 18 (10), 1074–1085.

Standard Test Methods for Coated and Laminated Fabrics for Architectural Use, D4851, 2019. ASTM.

Stein, M., Hedgepeth, J.M., 1961. Analysis of Partly Wrinkled Membranes. National Aeronautics and Space Administration, Washington.

Thomas, J.C., Wielgosz, C., 2004. Deflections of highly inflated fabric tubes. Thin-Walled Struct. 42 (7), 1049–1066.

Turner, A., Kabche, J., Peterson, M., Davids, W., 2008. Tension/torsion testing of inflatable fabric tubes. Exp. Tech. 32 (2), 47–52.

Veldman, S., 2006. Wrinkling prediction of cylindrical and conical inflated cantilever beams under torsion and bending. Thin-Walled Struct. 44 (2), 211–215.

Wan, Z., Cao, Z., Sun, Y., Fan, F., 2018. Pre-stressing method and structural behaviour of a Tensairity dome with multiple inflated cushions. Thin-Walled Struct. 132, 585–595.

Wan, Z., Cao, Z., Sun, Y., Fan, F., 2021. Experimental and numerical research on the structural behaviour of a Tensairity dome. Eng. Struct. 248, 113225.

Wang, C.-G., Tan, H.-F., Du, X.-W., He, X.-D., 2010. A new model for wrinkling and collapse analysis of membrane inflated beam. Acta Mech. Sin. 26 (4), 617–623.

Wang, C., Du, Z., Tan, H., 2012. Initial wrinkling and its evolution of membrane inflated cone in bending. Thin-Walled Struct. 59, 97–102.

Wang, X., Fu, H., Law, S., Yang, Q., Yang, N., 2020. Experimental study on the interaction between inner air and enveloping membrane of inflated membrane tubes. Eng. Struct. 219, 110892.

Wielgosz, C., Thomas, J.C., 2002. Deflections of inflatable fabric panels at high pressure. Thin-Walled Struct. 40 (6), 523–536.

Ye, Y., Gan, J., Liu, H., Guan, Q., Zheng, Z., Ran, X., Gao, Z., 2023. Experimental and numerical studies on bending and failure behaviour of inflated composite fabric membranes for marine applications. J. Mar. Sci. Eng. 11 (4), 800.

Ye, Y., Gan, J., Wu, W., Wang, S., Guedes Soares, C., 2024. Experimental and analytical assessment of the bending behaviour of floating inflated membrane beams. Ocean Eng. 314, 119710.

Ye, Y., Gan, J., Wu, W., Wang, S., Guedes Soares, C., 2025. Mechanical behaviour of rigid-flexible combined structures: aluminium-inflated membrane beams for application in floating photovoltaic platform. Thin-Walled Struct. 206, 112628.